Available online at www.dergipark.org.tr/en

INTERNATIONAL ADVANCED RESEARCHES and ENGINEERING JOURNAL

Journal homepage: www.dergipark.org.tr/en/pub/iarej

e-ISSN: 2618-575X

International Open Access

Volume 08
Issue 01

April, 2024

Research Article

An optimization study focused on lattice structured custom arm casts for fractured bones inspiring additive manufacturing

Mamoun Alshihabi [a,*] ***and Mevlüt Yunus Kayacan*** [a]

[a]*Isparta Univeristy of Applied Sciences, Mechanical Engineering Department, Isprta 33220, Turkey*

ARTICLE INFO

Article history:
Received 30 September 2023
Accepted 09 March 2024
Published 20 April 2024

Keywords:
Additive manufacturing
Arm cast
Finite element analysis
Johnson-cook model
Lattice structures

ABSTRACT

In case of fractures, cracks or damage to bone tissues, it is important to use casts, fixatives and protective equipment. Especially in cases where long-term use of casts is required, soft tissue wounds may occur in the human body due to their moisture and airtight structure. For this reason, the use of casts with custom designs, breathable materials, and high mechanical properties has become widespread in recent years. This study focuses on the design of custom arm casts using advanced additive manufacturing technologies and lightweight materials. By utilizing Voronoi lattice structures and hexagonal surface meshes, optimized designs adaptable to additive manufacturing were obtained from a standard arm cast. All cast geometries were investigated under 196 N and 380 N forces. Then, the impact of a 100 g and 1000 g concrete piece with a speed of 12.5 m/s on the arm cast was investigated. As a result of the analyzes, stress, impact plate velocities, deformation, strain and deformation energy were evaluated. The results showed that the designed arm casts have up to 60% better impact strength compared to conventional arm casts. Based on the findings of this study, the use of custom arm casts with optimized lattice structures designed for additive manufacturing will demonstrate high performance.

1. Introduction

Casting is a typical non-surgical procedure used to immobilize and stabilize shattered bones and promote normal healing [1]. It entails wrapping the wounded area in a stiff, hard substance to stabilize the bone, stop it from moving, and speed up the healing process [2]. Casts are often made of plaster or fiberglass and can be customized to fit the unique features of the injured limb or body part [3]. For many years, the application of casting to treat bone fractures has been a widely accepted and successful method. Casts not only assist in reducing pain and swelling, but also allow the broken bone to stay in a fixed position, promoting healthy bone formation. Accidents, falls, sports injuries, and underlying illnesses like osteoporosis are just a few of the causes of bone fractures [4]. Many fractures can be repaired without surgery utilizing techniques like casting, even though other fractures may necessitate surgical intervention [5]. Depending on the location and seriousness of the injury, different types of casts may be used for bone fractures. For instance, a short-arm cast, which covers the arm from the wrist to just below the elbow, may be necessary for a fractured arm [6]. On the other hand, a long-leg cast that covers the upper thigh and toes may be necessary for a fractured leg [7]. Depending on the situation, a cast may be necessary for a few weeks in certain instances or for several months in others [8]. After the cast is taken off, physical therapy is frequently suggested to assist the injured area regain its strength, flexibility, and range of motion [9].

For years, people have used casts to immobilize and stabilize fractured bones. They were made from materials like mud, clay, and tree bark. Casts were later developed in the middle of the 19th century and swiftly took over as the preferred method for treating bone fractures [10]. Casts were created by encircling the wounded limb or body part with wet strips of cast of Paris, which would subsequently harden and offer support. Fiberglass castings were created in the middle of the 20th century as a lighter, more pleasant alternative to cast of Paris since they were heavy and may irritate the skin [11]. A fiberglass material is wrapped around the wounded area to create a fiberglass cast, which is subsequently hardened by the application of synthetic resin [12]. Modern casts are frequently made utilizing additive manufacturing technologies to get a precise and cozy fit that is custom-made to the patient's demands [13].

* Corresponding author. Tel.: +90 537 2262 443.
E-mail addresses: mamounkhalshihabi@gmail.com *(M. Alshihabi)*, mevlutkayacan@isparta.edu.tr *(MY. Kayacan)*
ORCID: 0000-0002-9766-4465 *(M. Alshihabi)*, 0000-0003-3557-9537 *(MY. Kayacan)*
DOI: 10.35860/iarej.1369209

Furthermore, new materials like carbon fiber and thermoplastics have been created to make casts that are even lighter and stronger than conventional fiberglass casts. From the basic techniques of the past to the sophisticated, high-tech materials of the present, the development of casts used in bone fractures has come a long way [14]. These developments have improved casting as a therapy option for patients with bone fractures, making it safer, more efficient, and more comfortable.

Thermoplastic, fiberglass, and cast of Paris are common materials used to create modern arm casts. Because of its light weight, great strength, and stiffness, fiberglass is the material that is utilized the most frequently [15]. It can be shaped to the shape of the arm, giving a tight fit for the best immobilization. On the other hand, cast of Paris is more conventional and is occasionally still employed [16]. Although it takes longer to dry than fiberglass, it can offer a harder, more secure fit and it's a cheaper option than fiberglass. Thermoplastic castings are also growing in popularity since they are lightweight, waterproof, and can be heatedly molded for a customized fit [17]. Fiberglass casts are more resistant to breaking or cracking due to their higher tensile strength (305 MPa) and flexural modulus (17.2 GPa) in terms of mechanical qualities [18]. They are also less likely to bend or deform under load because to their higher flexural modulus. The cast of Paris, on the other hand, is better at absorbing shock and can distribute pressure more evenly across the arm while having a lower flexural modulus of 1.74 GPa and a much lower tensile strength of 2.76 MPa [19]. Thermoplastic casts have an impact strength of 130 J/m and an elastic modulus of 1.6 GPa, which is higher than plaster of Paris casts but lower than fiberglass. Because of their great impact strength, they are less prone to crack or break when dropped or bumped [20]. Additionally, they are more flexible and can more easily adapt to the curve of the arm due to their lower modulus of elasticity.

Arm cast production using additive manufacturing has been researched as an effective technique [21]. Compared to conventional casting methods, this technology has more design flexibility, customization, and shorter lead times [22]. A lightweight, custom-fitted cast that includes features like air holes and detachable components can be produced via 3D printing. Casts made using 3D printing have been demonstrated to be substantially lighter and more comfortable for patients while also having mechanical attributes that are comparable to those of conventional casts in terms of strength and rigidity [23]. Additionally, it has been discovered that using 3D printed casts with an open lattice structure improves airflow and lessens skin irritation [24]. Even if there are issues that need to be addressed, 3D printing for arm casts has promise. The price of 3D printing supplies and equipment, the length of time required for printing, and worries about bacterial development in the porous lattice structures are a few of these drawbacks [25]. Despite these difficulties, 3D printed casts are a viable solution for the future of arm casting due to their prospective advantages [26].

Six distinct prosthetic arm cast models were created for this study, covering the region from the wrist to just below the elbow. These models include two porous cast designs, three designs reinforced with a Voronoi surface lattice on their outer layer, and one original body design that has not been optimized. Each design has an own unique set of Voronoi point count and unique thicknesses. The size and shape of the resulting Voronoi cells are strongly influenced by the Voronoi point count, which is the distance between the generating points. The resulting Voronoi cells will be small and asymmetric if the generating points are close to one another [27]. In contrast, large, uniform Voronoi cells will develop if the generating points are spaced widely apart [28]. Modern arm casts can be a successful treatment for a variety of arm fractures and injuries, but they also have their own problems [29]. The inability to customize the cast, which can lead to a poor fit and limited functionality, is one of the most frequent issues. Longer healing times and increased suffering may result from this [30]. Another frequent problem is skin irritation and rashes brought on by a lack of airflow and moisture build-up inside the cast [31]. The restrictive nature of the cast can also cause stiffness and limited mobility, which can weaken the muscles and cause poor circulation [32]. Due to the difficulty in reaching the skin underneath the cast, maintaining proper hygiene and washing it might be difficult as well [33]. In this study, we aim to address these common issues by designing casts that are strong, stiff, lightweight, easy to manufacture, and to improve hygiene two porous designs were incorporated.

This innovative study makes a significant contribution to the existing literature on orthopedic care by addressing the shortcomings of traditional arm casts through the application of advanced additive manufacturing technologies. By incorporating Voronoi lattice structures and hexagonal surface meshes, the research optimizes custom arm cast designs for enhanced breathability, adaptability to additive manufacturing processes, and superior mechanical properties.

2. Materials and Methods

Designing an arm cast that is optimized for maximum effectiveness was the main goal of this research. To accomplish this, five different arm casts with different designs and parameters were created. On a real-life model of a human limb, first the design for the arm cast was created. This first step involved closely analyzing the arm's anatomical characteristics, including the size and shape of the bones and muscles as shown in Figure 1. Using this knowledge, A cast was created to offer the best possible

support and security while facilitating healthy recovery.

A thorough optimization procedure was then applied to the resulting design. To obtain the best results, The design was iteratively modified and improved using innovative modeling techniques, resulting in the production of five different optimized versions of the arm cast using this method, each with a distinctive set of parameters and features as shown in Figure 2. A collection of optimized arm casts was created, which has the potential to enhance patient outcomes and quicken the healing process by fusing in-depth anatomical knowledge with advanced modeling methods. This was achieved through the ability to use advanced modeling methods and incorporate in-depth anatomical knowledge.

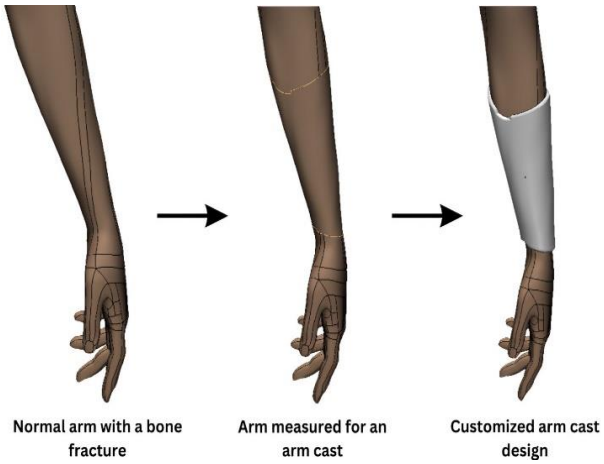

Figure 1. Process steps of the piece modeled from the broken arm

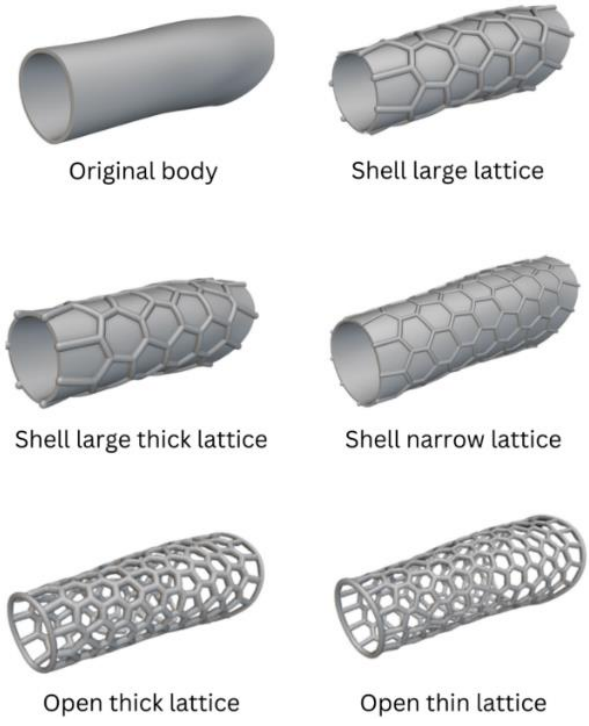

Figure 2. The optimized versions of the arm cast

With a thickness of 2 mm, the original arm cast design encompassed the region between the wrist and the elbow. Then, using nTopology, a program for 3D modeling and design optimization, this design was transformed into an implicit body. Implicit bodies, which are 3D geometries represented by a distance field, provide many advantages for design optimization [34]. Implicit bodies have several advantages over conventional CAD geometry, including greater flexibility and simplicity of manipulation. Additionally, they can be utilized to quickly and simply create a variety of design variations.

After the initial design was transformed into an implicit body, it was optimized to produce five distinct iterations of the arm cast. Three of these designs were based on the original body but had a Voronoi surface lattice reinforced on their outer surface. The shell large lattice 2 mm which is the first design comprised a lattice thickness of 6 mm, 50 Voronoi points, and 1 random seed. The second design that's named the shell large lattice 3 mm similar to the first, had a Voronoi point count of 50, a random seed of 1, and a lattice thickness of 6 mm. The original body's thickness, however, was increased to 3 mm. The third design which is the shell narrow lattice 2 mm had a lattice thickness of 3 mm, 100 Voronoi points, and one random seed. The fourth design which is the open large lattice 2 mm is a porous arm cast with a lattice thickness of 7 mm, 130 Voronoi points, and a random seed of 1. The fifth design which is the open narrow lattice 2 mm is a porous arm cast with a lattice thickness of 5 mm, 160 Voronoi points, and a random seed of 1. All of these parameters are shown in Figure 3 and listed in Table 1 where each design has been assigned a letter to be read easier.

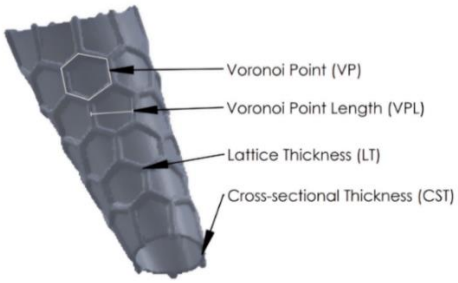

Figure 3. Lattice parameters

Table 1. nTopology design parameters

Arm cast type	Voronoi point count	Voronoi point length	Lattice thickness	Cross-sectional thickness
(**A**) Original body	none	-	-	2 mm
(**B**) Shell large lattice	50	30 mm	6 mm	2 mm
(**C**) Shell large thick lattice	50	30 mm	6 mm	3 mm
(**D**) Shell narrow lattice	100	15 mm	3 mm	2 mm
(**E**) Open thick lattice	130	12 mm	7 mm	2 mm
(**F**) Open thin lattice	160	12 mm	5 mm	2 mm

These improved designs provided a variety of solutions for various needs and preferences, with the goal of enhancing the arm cast's practicality and effectiveness. The two porous arm cast designs were made using the Voronoi surface lattice block. In contrast to the other ideas, this one included generating a surface lattice from the part's outside mesh without fusing the lattice to the original body. To ensure porosity, the lattice was maintained separately. To retain the arm cast's functionality, rims for the entrance and exit have to be designed. This was addressed by the addition of circular rims to both porous designs. These rims served as both a solid foundation for the lattice and a distinct boundary for the entrance and exit of the arm cast. After completing the designs they were exported from nTopology as mesh STL files each design was exported with a different mesh tolerance as they are not all similar. Some of them were exported with the mesh tolerance of 1.5 mm and some of them were exported with the tolerance 2.5 mm but the common factor between all of them is that all their meshes were simplified prior to exporting. The next step was to analyze the designs behaviours under different boundary conditions so for each design a static structural analysis and an explicit dynamics analysis was made. In the static structural analysis each design was fixed in a vertical line on the bottom of the arm cast and two forces were applied seperately on top of the cast in the exact opposite way of the fixed area as shown in Figure 4. The first force was 196 N and the second force was 380 N. after applying the forces and fixing the bottom the eqivalent Von-mises stress, the equivalent elastic strain and total deformation values were analyzed for each design.

To analyze the behavior of the cast designs after an impact, an explicit dynamics simulation was conducted on ANSYS Workbench. This involved dropping a concrete block onto the upper surface of the cast at a velocity of 12.5 m/s, using two different masses of 0.1 kg and 1 kg respectively with having a fixed support in a vertical line on the bottom face of the cast as shown in Figure 5. To carry out the simulation, all the cast designs were exported as meshes from nTopology and then imported into SolidWorks. then a rectangular extruded solid block was designed and positioned 0.5 mm above the upper surface of the arm cast, which was dropped onto the cast at the same velocity of 12.5 m/s.

The mathematical relationships used with ANSYS Workbench are presented within the scope of the study. In order to calculate explicit dynamics with Ansys, the following Eq. 1 was used.

$$y(t_{n+1}) = y(t_n) + \Delta t \dot{y}(t_n) \quad (1)$$

Eq. 2 calculates the directional strains along X axis. Note that directional strain is a measure of how much an object deforms or stretches along a specific axis.

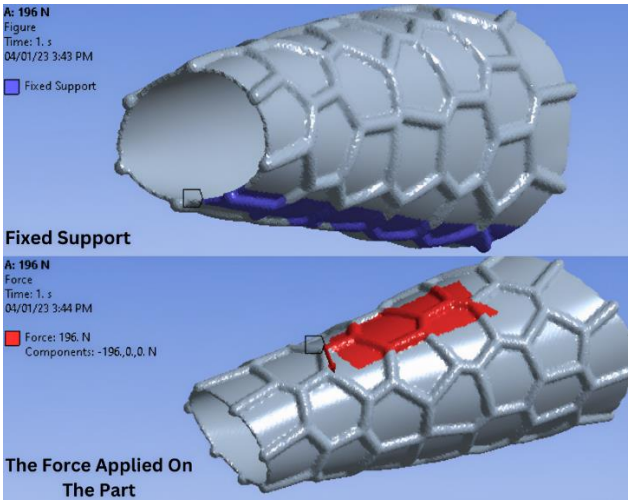

Figure 4. Boundary conditions of the static analysis

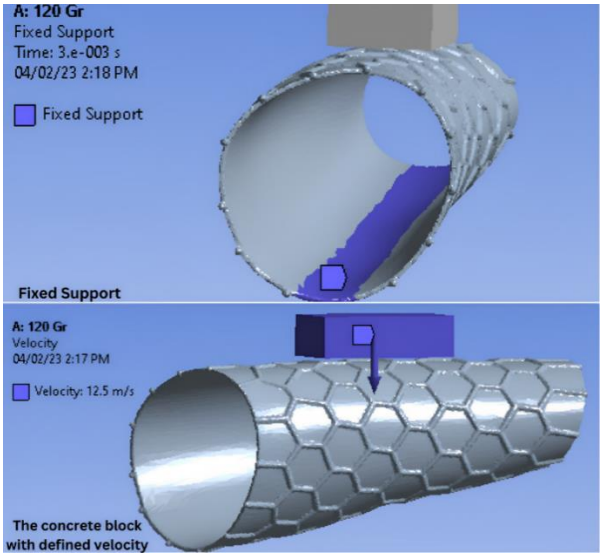

Figure 5. Boundary conditions of the explicit dynamics analysis

$$\varepsilon x = \left(\frac{\Delta Hx}{H}\right) \quad (2)$$

Eq. 3 is based on the principle of the work-energy theorem, which states that the work done on an object is equal to the change in its kinetic energy. In this case, the work done on the object is assumed to be due to a resistive force (such as friction) that causes the object to slow down from an initial velocity to a final velocity. The amount of kinetic energy lost by the object is proportional to the square of the velocity difference ($vi^2 - vf^2$) and the mass of the object (m).

$$\Delta KE = \left(\frac{1}{2}\right) * m * (vi^2 - vf^2) \quad (3)$$

Eq. 4 relates the reduction in kinetic energy of a material due to a directional strain in a particular direction so it's directional strain*kinetic energy reduction.

$$SK = \varepsilon * \Delta KE \quad (4)$$

Eq. 5 relates the reduction in kinetic energy of a material due to a specific strain in a particular direction so it's specific strain*kinetic energy reduction.

$$SSK = \left(\frac{\Delta L}{L0}\right) * (\varepsilon * \Delta KE) \quad (5)$$

According to the Courant-Friedrichs-Lewy (CFL) situation, the time steps needed depending on the unit mesh size were determined according to Eq. 6. "h" is characteristic length of a finite elements, "c" is wave speed in the material, "f" is safety factor as f≤1.

$$\Delta t \leq f \left[\frac{h}{c}\right]_{min} \quad (6)$$

Longitudinal Wave Speed value was obtained for materials according to Eq. 7. "E" is young's modulus and "ρ" is density. [35]

$$c = \sqrt{\frac{E}{\rho}} \quad (7)$$

Basically, eigenvalue approaches were used in the calculations of the modal analysis according to Eq. 8. [M] is mass matrix and [K] is stiffness matrix. $[K] - \omega_i^2[M]$ is definition of natural frequencies and $\{\varphi\}_i$ is mode shapes.

$$[K] - \omega_i^2[M]\{\varphi\}_i = \{0\} \quad (8)$$

Strain-rate hardening is represented by the equation, where K is the strain-rate hardening coefficient, and n is the strain-rate hardening exponent.

$$\sigma = K\,\varepsilon^{n+1} \quad (9)$$

Damage evolution is described by the equation, where D is the damage variable, A is the damage coefficient, and m is the damage exponent.

$$D = 1 - \exp(-A\,\varepsilon^m) \quad (10)$$

The stress-strain relationship is an equation, where σ is the stress in the material, E is the Young's modulus of elasticity, and ε is the strain in the material.

$$\sigma = E\,\varepsilon \quad (11)$$

The contact forces equation, where f_c is the contact force, K_c is the contact stiffness, Δu_n is the normal displacement, μ is the friction coefficient, f_n is the normal force, and Δu_t is the tangential displacement.

$$f_c = K\,c\,\Delta u_n + \mu\, f_n \Delta u_t \quad (12)$$

The equation that represents the stress in the Johnson-Cook model is shown in Eq. 13. where σ_F represents the flow stress of the material A describes the yield stress of the material under reference conditions B is the strain hardening constant ε_{pn} denotes the equivalent plastic strain ε_p is the plastic strain rate ε_0 is the reference strain rate C is the strengthening coefficient of strain rate T represents the temperature m is the thermal softening coefficient of the model (in case of thermal effect consideration). [36]

$$\sigma F = (A + B \cdot \varepsilon p_n) \cdot \left(1 + \frac{\varepsilon_p}{\varepsilon_0}\right) C.(1 - T^m) \quad (13)$$

The following equation represents the relationship between the flow stress and the defined strain rates and temperature-dependent flow curves. here σF is the flow stress k_1 is the Johnson-Cook material constant that describes the yield stress of the material under reference conditions ε_p is the equivalent plastic strain $\dot{\varepsilon}_p$ is the equivalent plastic strain rate k_t is the Johnson-Cook material constant that describes the strain hardening behavior of the material T is the temperature k_e is the Johnson-Cook material constant that describes the damage behavior of the material D is the damage variable.

$$\sigma F = k^1(\varepsilon_p, \dot{\varepsilon}_p) \cdot k_t(\varepsilon_p, T) \cdot k_e(D) \quad (14)$$

In the impact tests, the damage mechanisms of the materials were calculated according to the equation of state (EOS) principle and the following Eq. 15 was used.

$$P = K_1\mu + K_2\mu^2 + K_3\mu^3 \quad (15)$$

The behavior of PLA (polylactic acid) under high strain rates and temperatures has been predicted using the Johnson-Cook model and PLA's characteristics. Thermoplastic known as PLA is biodegradable and renewable, and it is used in additive production among other sectors. Making arm casts out of PLA materials is a great application for additive manufacturing. The mechanical behavior of PLA under various loading scenarios, including tension, compressive, and shear loading, has been studied using the Johnson-Cook model which it's properties can be seen in Table 2. This is crucial when designing and enhancing the mechanical qualities of PLA-based products, such as arm casts, to satisfy the demands of the particular application.

Fused Deposition Modeling (FDM), Stereolithography (SLA), and Selective Laser Sintering (SLS) are a few techniques for 3D printing with PLA [38,39]. The most popular and reasonably priced PLA printing technique is FDM. The PLA filament used by FDM printers is melted and pushed through a tiny nozzle. The melted filament is then deposited by the printer in layers, building the item. The most economical way to print with PLA is through FDM because PLA is a reasonably inexpensive substance for 3D printing. The price of 3D printing with PLA, however, can vary significantly based on the size and complexity of the object as well as the caliber and features of the 3D printer being used.

Table 2. Properties of the material of the Johnson-Cook model [37].

Property	Value	Unit
Density	1240	kg/m³
Isotropic Elasticity (PLA)	**Value**	**Unit**
Young's Modulus	4.1	GPa
Poisson's Ratio	0.35	
Bulk Modulus	6.05	GPa
Shear Modulus	1.58	GPa
Yield Strength	62.7	MPa
Johnson Cook Strength	**Value**	**Unit**
Initial Yield Stress	0.2	GPa
Hardening Constant	0.45	GPa
Hardening Exponent	0.2	
Strain Rate Constant	5	
Reference Strain Rate	1	

3. Results and Discussion

During the static analysis, the behavior of each design was thoroughly examined under two different load conditions. The first load was fixed at 196 N, and the second was 380 N. The focus of the study was on calculating the elastic strain, total deformation, and Von Mises stress values for each design. The equivalent stress values for each design under the 380 N force pressure are shown graphically in Figure 6. This information is essential for comprehending how each design reacts to outside loads and can guide choices regarding which design is most appropriate for particular uses. By examining the equivalent stress values, more information can be obtained regarding the possible strength and durability of each design.

Bar graphs were produced to demonstrate the results of the static analysis, showing the stress, strain, and deformation values for each design. These graphs give a thorough summary of the stress, strain, and deformation that each component underwent while operating within the previously mentioned boundary conditions. To emphasize the differences between the outcomes of each design, A method of comparison was used to represent each graph as a specific design. By comparing the graphs, the advantages and disadvantages of each design were determined, and more information was obtained about how they fared under the specified load circumstances.

First, a stress bar graph was constructed using data from each of the six parts. In order to make it simple to compare the various components, stress values from each design were chosen and plotted on a single graph. To show the findings of the static analysis under the two different load conditions, a bar graph was created. The graph as shown in Figure 7, depicts how each design behaves when subjected to a force of 196 N and 380 N.

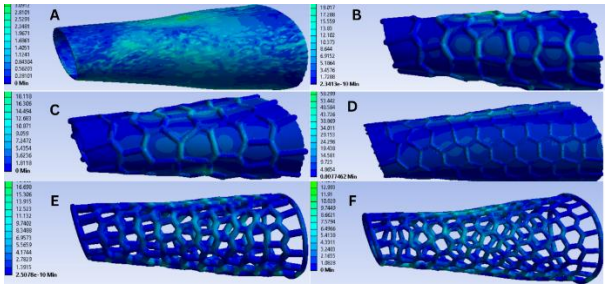

Figure 6. Von-Missses Stresses in MPa under 380 N of force

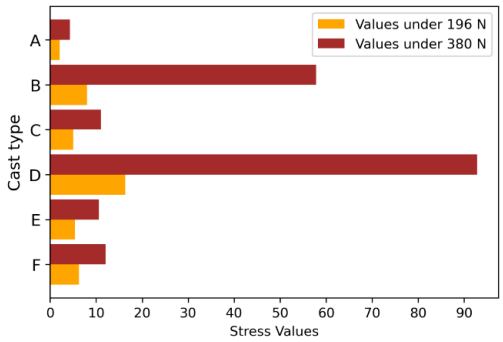

Figure 7. Maximum stress in MPa under 196 and 380 N of load

As seen in Figure 7 the open thin lattice (marked as F) showed a 2043.25% increase under 380 N of load which is a huge increase in stress values and the shell large lattice 2 mm (marked as B) showed a 1234.66% increase under 380 N of load which is also a very big increase in stress values which means these designs may not be durable compared to the other designs. In a similar study where the cast was subjected to only 30 N of load, the design experienced a maximum stress of 13.69 MPa. In contrast, the design D which showed the most stress and was subjected to a higher load of 196 N, experienced a maximum stress of approximately 18 MPa. However, when recalculating design D's stress as if it were subjected to the same 30 N load, the stress reduces to 2.75 MPa. When considering the difference in load conditions, designs in this study demonstrate superior stress resistance, highlighting their robustness in comparison to the aforementioned study [40]. Selecting strain data from each of the six parts, a strain bar graph was made. This graph has the maximum strain values from each design drawn on it to make it simple to compare the various components. It was made to display the results of the static analysis under the two different load circumstances. The maximum strain of each design is depicted in the graph in Figure 8 when the parts are subjected to a force of 196 N and 380 N.

In Figure 8 the shell narrow lattice (marked as D) showed 5262.6% increase in maximum strain values under 196 N of load and 3296.42% increase in maximum strain values under 380 N of load.

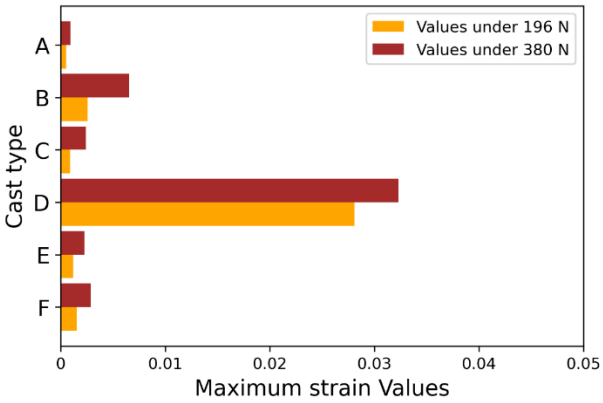

Figure 8. Maximum strain under 196 and 380 N of load

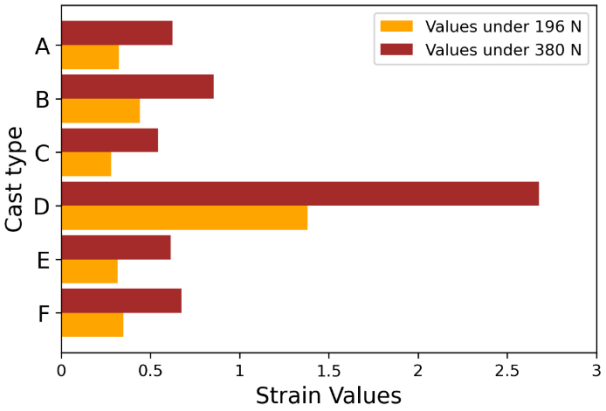

Figure 9. Deformation in mm under 196 and 380 N of load

A bar graph was created using information from all six designs to depict the overall deformation each component underwent during the static analysis. A visual representation that enables simple comparison between the various components by selecting the total deformation values from each design was created and plotted on a single graph. The results of the static analysis under the two different load circumstances were represented by the graph in shown in Figure 9 which shows strain values under a force of 196 N and 380 N.

In Figure 9 the shell narrow lattice (marked as D) yet again has proven to be not durable as it experienced the most deformation out of the other designs. It showed a 328.727% increase of deformation values under 196 N of load when compared to original body and It showed a 328.741% increase in deformation values under 380 N of load when compared to the original body. Based on the deformation distribution, the shell narrow lattice design exhibits significant deformation in some areas, indicating that this design is prone to deform under the applied load. This deformation renders the design unsuitable for use as an arm cast because it could pose a risk of harm to the patient's hand. It is important to note that the excessive deformation observed in the shell narrow lattice design is likely due to both its geometry and the specific load conditions applied during the analysis.

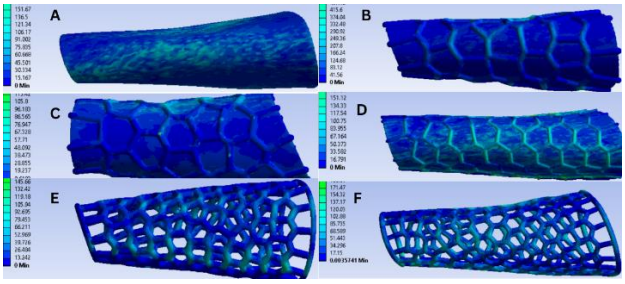

Figure 10. Von-Missses Stresses in MPa after impact with 1 kg concrete block

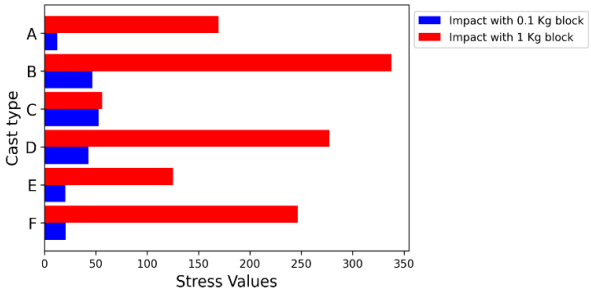

Figure 11. Von-mises stress in MPa for different impact scenarios on each part

Also, the open thick lattice and the shell large lattice 3 mm showed great results as the deformation values that were shown meant that these two cast types undergo very little deformation which protects the patient's arm from any impact. During the explicit dynamics analysis, The behavior of each design was investigated after dropping two different concrete blocks. The first block had a mass of 0.1 kg, and the second had a mass of 1 kg. During the analysis, the focus was on calculating the elastic strain, total deformation, and Von Mises stress values for each design. The equivalent stress values for each design under the 1 kg block are depicted in Figure 10. This information is crucial for understanding how each design responds to external loads and can aid in determining which design is best suited for specific applications. By examining the equivalent stress values, Insight into the potential strength and durability of each design can be gained through this analysis.

Bar graphs have been created to display the outcomes of the explicit dynamics analysis. These graphs make it simple to compare the numbers and results of the different parts and to understand how they behave. To show the stress values of each part in response to two distinct impact scenarios involving concrete blocks, a bar graph in particular has been made. The first the block weighs 0.1 kilograms, while the second block weighs 1 kilogram. This bar graph is shown in Figure 11.

As seen in Figure 11 the open thick lattice (marked as E) showed a 26.11% decrease in stress compared to the original body for the 1 kg impact analysis. And the shell large lattice 3 mm (marked as C) showed a 66.87% decrease in stress compared to the original body for the 1 kg impact analysis. The strain values of each component

under two different impact situations using concrete blocks have been displayed in an another bar graph. Figure 12's graph provides a clear and concise illustration of how each component responds to various levels of mass and impact and gives strain values to better understand the behavior of each part.

As seen in Figure 12 yet again the open thick lattice (marked as E) showed a 44.07% decrease in maximum strain when compare to the original body for 1 kg impact analysis. A 44.07% decrease in maximum strain value for an optimized part when compared to the original part indicates a significant improvement in the part's performance. In Figure 13 the total deformation values for all six parts are shown in a bar graph for both impact masses of 0.1 kg and 1 kg. The graph shows the strength of the open thick lattice (marked as E) and the shell large lattice 3 mm (marked as C) and how durable and strong these two parts are while on the other hand the shell narrow lattice yet again proved unsuitable as an arm cast because of the high level of deformation it shows. Compared to the original body.

All 5 optimized designs showed better deformation values than the original part but the open thick lattice (marked as E) and the shell large lattice 3 mm (marked as C) yet again showed a very significant reduction in deformation values for the 1 kg impact analysis as the open thick lattice showed a 53.96% decrease and the shell large lattice showed a 40.41% decrease. And in the 0.1 kg analysis the open thick lattice showed a 45.73% decrease. A velocity change line graph for each part for the impact with two different concrete blocks with the masses of 0.1 kg and 1 kg makes understanding the analysis better by showing how the velocity of a material changes over time due to an impact. Figure 14 and Figure 15 show the velocity changes of the concrete block for all the six designs.

When the plate velocities were analyzed, it was determined that open thick lattice (marked as E) and shell large lattice 3 mm lattice (marked as C) cast designs showed the best results. All lattice designs showed better results than the original body. As can be seen from the reduction in the velocities of the impacting plates, it is seen that the lattice structures have significant effects on impact damping. Impact energy calculations are crucial to impact analysis because they offer insightful knowledge into how materials behave under increased stress. The kinetic energy of the system is transferred during a collision, which causes the colliding objects to deform or sustain harm. The quantity of energy transferred during a collision and its impact on the objects are quantified with the aid of impact energy calculations. While directional strain refers to the direction of the deformation, specific strain refers to the amount of deformation that takes place in a particular region of the material.

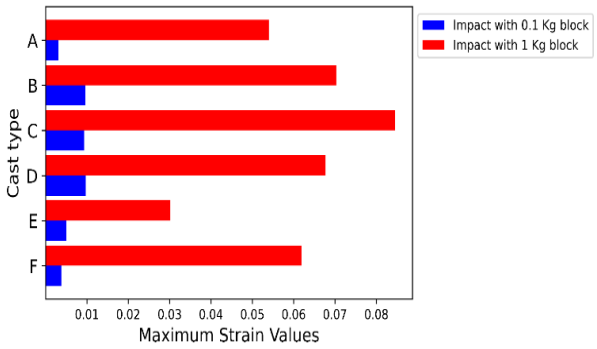

Figure 12. Strain for different impact scenarios on each

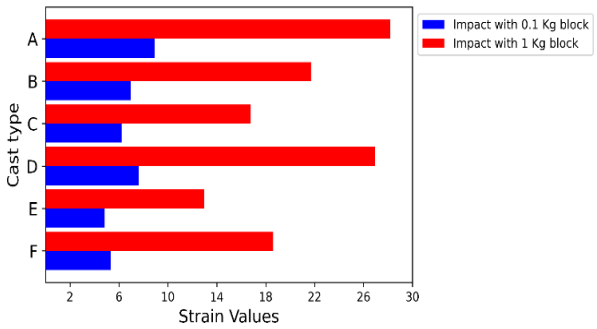

Figure 13. Deformation in mm for different impact scenarios on each part

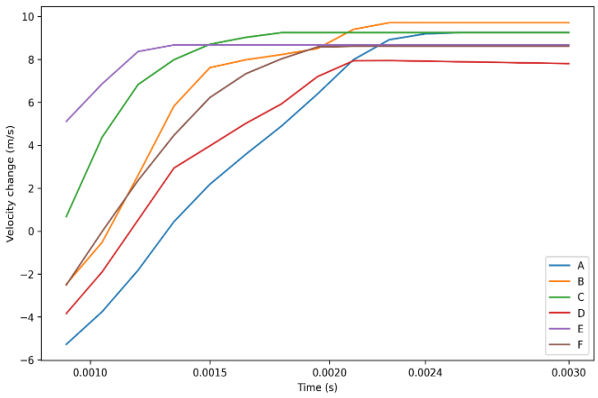

Figure 14. Velocity change line graph for all parts under 0.1 kg impact

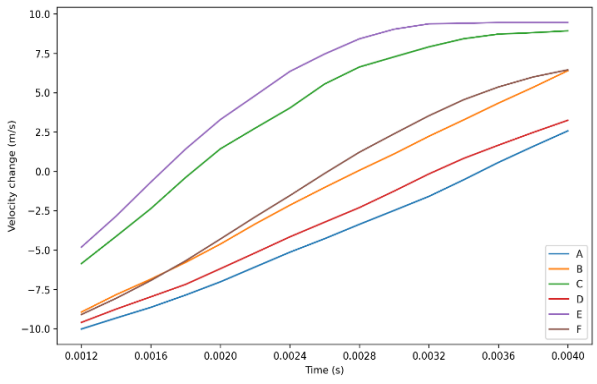

Figure 15. Velocity change line graph for all parts under 1 kg impact

In order to anticipate how materials will behave in upcoming impacts, it is essential to understand the specific and directional strain. Figure 16 shows the Kinetic energy reduction to directional strain values for each design for both 0.1 kg and 1 kg analyzes.

A graph of the kinetic energy against the specific strain was created to better comprehend how a material or structure behaves when it is deformed. A material experiences deformation or strain as a result of external pressures or loads, which lowers its kinetic energy. A graph depicting the relationship between the two variables was acquired by plotting the decrease in kinetic energy against the specific strain, which is the quantity of deformation per unit length or area. This graph can be used to build structures that won't fail under loads and deformations. The strength, stiffness, and ductility of the material properties that are crucial for creating effective and secure structures can be examined by analyzing the graph in Figure 17.

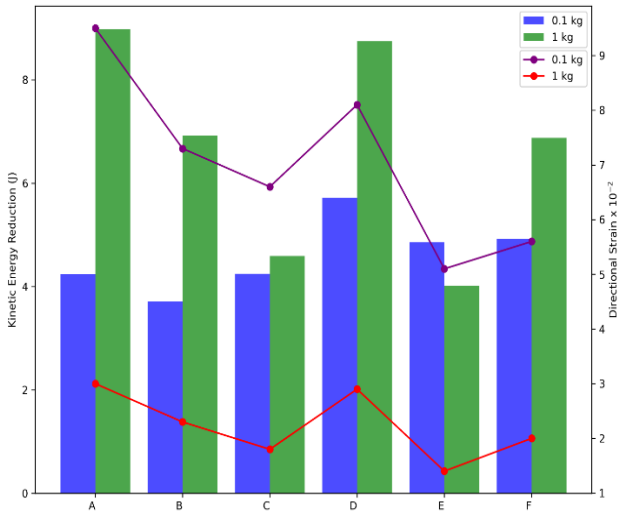

Figure 16. Kinetic energy reduction to directional strain

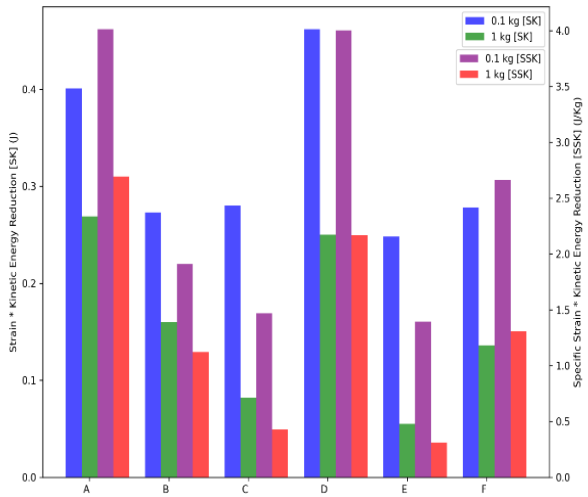

Figure 17. Kinetic energy reduction and energy analysis depending on specific strain

4. Conclusions

Within the scope of this study, the focus was on the optimization of casts of conventional designs with design parameters suitable for additive manufacturing. In this regard, hexagonal Voronoi lattice structures are designed volumetrically and superficially. All designs are analyzed under static loads of different strengths and under the impact of concrete blocks of different weights. According to the results of the analyzes, important findings are as follows:

- Under static loads, the original body is more advantageous in terms of stress and strain, whereas the lattice designs are advantageous in terms of deformations. It is important that a cast does not exert pressure on the damaged arm bone by deforming at the lowest level.
- In the case of impact of concrete blocks, open thick lattice and shell large lattice 3 mm casts gave good results in terms of stress, strain and deformations. It was understood that the lattice structures showed improved properties in impact moments.
- It was found that open thick lattice and shell large lattice 3 mm casts can reduce the impact velocities of concrete parts much faster. This may help to reduce the effects of the impact in a short time and prevent the pressure on the broken arm bone.
- Up to 85% lower SK and SSK data were obtained. It is understood that the rate of energy absorbed will increase with lower strain and kinetic energy drop. While the deformation change in gypsum is low, the rebound rate of the concrete block is also very high. In this way, the collision effect could be prevented effectively and quickly.

In future studies, customized cast design optimizations can be performed by using different lattice structures. Finite element analysis will be focused on the verification of the modelled casts by experimental methods.

Declaration

The author(s) declared no potential conflicts of interest with respect to the research, authorship, and/or publication of this article. The author(s) also declared that this article is original, was prepared in accordance with international publication and research ethics, and ethical committee permission or any special permission is not required.

Author Contributions

In the scope of this study, Author 1 was the executor of the ideas, the optimizer of design, the creator of the analyses, concluder of results and writer of article. Author 2 was the creator of the idea, design boundary conditions and literature review and concluder of results.

References

1. Kastenberger, T., Kaiser, P., Schmidle, G., Schwendinger, P., Gabl, M., and Arora, R., *Arthroscopic assisted treatment of distal radius fractures and concomitant injuries*. Archives of Orthopaedic and Trauma Surgery, 2020. **140**: p. 623-638.
2. Fang, Y., Yang, X., Lin, Y., Shi, J., Prominski, A., Clayton, C., and Tian, B. *Dissecting biological and synthetic soft–hard interfaces for tissue-like systems*. Chemical Reviews, 2021. **122**(5): p. 5233-5276.
3. Root, S. E., Sanchez, V., Tracz, J. A., Preston, D. J., Zvi, Y. S., Wang, K., and Whitesides, G. M., *An Expanding Foam-Fabric Orthopedic Cast*. Advanced Materials Technologies, 2022. **7**(9): p. 2101563.
4. Craig, J., Clarke, S., and Moore, P, *Orthopaedic and Trauma Nursing: An Evidence-based Approach to Musculoskeletal Care*. Principles of Fracture Management, 2023. p. 240-255.
5. Leixnering, M., Rosenauer, R., Pezzei, C., Jurkowitsch, J., Beer, T., Keuchel, T., and Quadlbauer, S, *Indications, surgical approach, reduction, and stabilization techniques of distal radius fractures*. Archives of Orthopaedic and Trauma Surgery, 2020. **140**: p. 611-621.
6. Dib, G., Maluta, T., Cengarle, M., Bernasconi, A., Marconato, G., Corain, M., and Magnan, B, *Short arm cast is as effective as long arm cast in maintaining distal radius fracture reduction: Results of the SLA-VER noninferiority trial*. World Journal of Orthopedics, 2022. **13**(9): p. 802.
7. Sabeh, K., Aiyer, A., Summers, S., and Hennrikus, W., *Cast application techniques for common pediatric injuries: A review*. Current Orthopaedic Practice, 2020. **31**(3): p. 277-287.
8. Farrell, S., Schaeffer, E. K., and Mulpuri, K., *Recommendations for the care of pediatric orthopaedic patients during the COVID pandemic*. The Journal of the American Academy of Orthopaedic Surgeons, 2020. **28**(11): p. 477– 486.
9. Byrchak, V., Duma, Z., and Aravitska, M., *Effectiveness of the active physical therapy in restoring wrist and hand functional ability in patients with immobility-induced contracture of the wrist joint complicated by median nerve entrapment owing to distal forearm fracture*. Journal of Physical Education and Sport, 2020. **20**(6): p. 3599-3606.
10. Marin, E., Boschetto, F., and Pezzotti, G., *Biomaterials and biocompatibility: An historical overview*. Journal of Biomedical Materials Research Part A, 2020. **108**(8): p. 1617-1633.
11. Rezaei, R., *The Easy Wrap Orthopedic Cast*, Rochester Institute of Technology, 2017.
12. Varivodov, V. N., Kovalev, D. I., Zhulikov, S. S., Golubev, D. V., Romanov, V. A., and Mirzabekyan, G. Z., *Technological aspects of the use of cast polymer insulation for high-voltage switchgear and busbars*. Power Technology and Engineering, 2021. **54**: p. 915-922.
13. Paterson, A. M., Bibb, R., Campbell, R. I., and Bingham, G., *Comparing additive manufacturing technologies for customised wrist splints*. Rapid Prototyping Journal, 2015. **21**(3): p. 230-243.
14. Henkel, J., Woodruff, M. A., Epari, D. R., Steck, R., Glatt, V., Dickinson, I. C., and Hutmacher, D. W., *Bone regeneration based on tissue engineering conceptions—a 21st century perspective*. Bone research, 2013. **1**(1): p. 216-248.
15. Iftekhar, A., *Standard handbook of biomedical engineering and design*. Biomedical composites, 2004. p. 1-17.
16. Edwards, M. A, *Guide to Modelling in Clay and Wax: And for Terra Cotta, Bronze and Silver Chasing and Embossing, Carving in Marble and Alabaster, Moulding and Casting in Cast-Of-Paris or Sculptural Art Made Easy for Beginners*. Read Books Ltd, 2016.
17. Maji, P., and Naskar, K., *Styrenic block copolymer-based thermoplastic elastomers in smart applications: Advances in synthesis, microstructure, and structure–property relationships—A review*, Journal of Applied Polymer Science, 2022. **139**(39): p. 52942.
18. Gogoi, R., Niyogi, U. K., Alam, M. S., and Mehra, D. S, *Study of effect of NCO/OH molar ratio and molecular weight of polyol on the physico-mechanical properties of polyurethane cast*. World Applied Sciences Journal, 2013. **21**(2): p. 276-283.
19. Parmar, A. J., Tyagi, S. K., Dabas, V. S., Mistry, J. N., Jhala, S. K., Suthar, D. N., and Bhatti, I. M., *Assessment of the physical and mechanical properties of cast of Paris bandage cast used as a splinting and casting materials*. Veterinary World, 2014. **7**(12): p. 1123-1126.
20. Gibson, I., Rosen, D., Stucker, B., Khorasani, M., Gibson, I., Rosen, D., and Khorasani, M., *Materials for additive manufacturing*. Additive Manufacturing Technologies, 2021. p. 379-428.
21. Hasanov, S., Alkunte, S., Rajeshirke, M., Gupta, A., Huseynov, O., Fidan, I., and Rennie, A., *Review on additive manufacturing of multi-material parts: progress and challenges*. Journal of Manufacturing and Materials Processing, 2021. **6**(1): p. 4.
22. Pal, A. K., Mohanty, A. K., and Misra, M., *Additive manufacturing technology of polymeric materials for customized products: recent developments and future prospective*. RSC Advances, 2021. **11**(58): p. 36398-36438.
23. Banga, H. K., Kumar, R., Channi, H. K., and Kaur, S., *Parametric design and stress analysis of 3D printed prosthetic finger*. In Innovative Processes and Materials in Additive Manufacturing, 2023. p. 57-80.
24. Zolfagharian, A., Gregory, T. M., Bodaghi, M., Gharaie, S., and Fay, P., *Patient-specific 3D-printed splint for mallet finger injury*. International Journal of Bioprinting, 2020. **6**(2): p. 259.
25. Peng, S., Guo, Q., Thirunavukkarasu, N., Zheng, Y., Wang, Z., Zheng, L., and Weng, Z., *Tailoring of photocurable ionogel toward high resilience and low hysteresis 3D printed versatile porous flexible sensor*. Chemical Engineering Journal, 2022. **439**: p. 135593.
26. Richa, S., Bhaskar, J., and Kumar, A., *A Review on: 3D Printed Orthopaedic Cast for Improved Forearm Fracture*

Rehabilitation. International Journal for Research in Applied Science & Engineering Technology, 2021. **9**(11): p. 66-72.

27. Lei, H. Y., Li, J. R., Xu, Z. J., and Wang, Q. H., *Parametric design of Voronoi-based lattice porous structures*. Materials and Design, 2020. **191**: p. 108607.
28. Bukenberger, D. R., Buchin, K., and Botsch, M., *Constructing L∞ Voronoi Diagrams in 2D and 3D.* In Computer Graphics Forum, 2022. **41**(5): p. 135-147.
29. Shirley, E. D., Maguire, K. J., Mantica, A. L., and Kruse, R. W., *Alternatives to traditional cast immobilization in pediatric patients*. JAAOS-Journal of the American Academy of Orthopaedic Surgeons, 2020. **28**(1): p. 20-27.
30. Graham, J., Wang, M., Frizzell, K., Watkins, C., Beredjiklian, P., and Rivlin, M., *Conventional vs 3-dimensional printed cast wear comfort*. Hand, 2020. **15**(3): p. 388-392.
31. Williams, R. J., *Exploring thermal discomfort amongst lower-limb prosthesis wearers*. UCL University College London, 2020.
32. Craig, J., Clarke, S., and Moore, P., *Orthopaedic and Trauma Nursing: An Evidence-based Approach to Musculoskeletal Care*. Principles of Fracture Management, 2023. p. 240-255.
33. Gao, Y., Yu, L., Yeo, J. C., and Lim, C. T., *Flexible hybrid sensors for health monitoring: materials and mechanisms to render wearability*. Advanced Materials, 2020. **32**(15): p. 1902133.
34. Patel, A. H., Baxi, N. J., and Gurrala, P. K., *A study on triply periodic minimal surfaces: A case study*. Materials Today: Proceedings, 2022. **62**: p. 7334-7340.
35. Satkar, A. R., Mache, A., and Kulkarni, A., *Numerical investigation on perforation resistance of glass-carbon/epoxy hybrid composite laminate under ballistic impact*. Materials Today: Proceedings, 2022. **59**: p. 734-741.
36. Aslam, M. A., Ke, Z., Rayhan, S. B., Faizan, M., and Bello, I. M., *An investigation of soft impacts on selected aerospace grade alloys based on Johnson-Cook Material Model.* In Journal of Physics: Conference Series, 2020. **1707**(1): p. 012008.
37. Pinto, V.C., Ramos, T., Alves, S., Xavier, J., Tavares, P., Moreira, P.M.G.P. and Guedes, R.M., *Comparative failure analysis of PLA, PLA/GNP and PLA/CNT-COOH biodegradable nanocomposites thin films*. Procedia Engineering, 2015. **114**: p.635-642.
38. Tanabi, H., *Investigation of the temperature effect on the mechanical properties of 3D printed composites*. International Advanced Researches and Engineering Journal, 2021. **5**(2): p. 188-93.
39. Bolat, ç., And ergene, b., *An experimental effort on impact properties of polylactic acid samples manufactured by additive manufacturing*. Düzce Üniversitesi Bilim ve Teknoloji Dergisi, 2023. **11**(2): p. 998-1013.
40. Mian, S.H., Umer, U., Moiduddin, K. and Alkhalefah, H., *Finite Element Analysis of Upper Limb Splint Designs and Materials for 3D Printing*. Polymers, 2023. **15**(14): p. 2993.